Author: Mao, Junjie
Title: Astrophysical plasma modeling of the hot Universe : advances and challenges in high-resolution X-ray spectroscopy
Date: 2018-06-07

6

Photoionized emission and absorption features in the high-resolution X-ray spectra of NGC 3783

Junjie Mao, M. Mehdipour, J. S. Kaastra, E. Costantini, C. Pinto, G. Branduardi-Raymont, E. Behar, U. Peretz, S. Bianchi, G. A. Kriss, G. Ponti, B. De Marco, P.-O. Petrucci, L. Di Gesu, R. Midde, J. Ebrero and N. Arav

Our *Swift* monitoring program triggered two joint *XMM-Newton*, *NuSTAR* and HST observations on 11 and 21 December 2016 targeting NGC 3783, as its soft X-ray continuum was heavily obscured. Consequently, emission features, including the O VII radiative recombination continuum, stand out above the diminished continuum. We focus on the photoionized emission features in the December 2016 RGS spectra, and compare them to the time-averaged RGS spectrum obtained in 2000–2001 when the continuum was unobscured. A two-phase photoionized plasma is required to account for the narrow emission features. These narrow emission

This chapter has been submitted to Astronomy & Astrophysics, 2018

features are weakly varying between 2000–2001 and December 2016. We also find a statistically significant broad emission component in the time-averaged RGS spectrum in 2000–2001. This broad emission component is significantly weaker in December 2016, suggesting that the obscurer is farther away than the X-ray broad-line region. In addition, by analyzing the archival high-resolution X-ray spectra, we find that nine photoionized absorption components with different ionization parameters and kinematics are required for the warm absorber in X-rays.

6.1. Introduction

The optical spectra of Seyfert 1 galaxies often show broad emission lines with a velocity broadening of a few 10^3 km s^{-1} and narrow emission lines with a velocity broadening about a few 10^2 km s^{-1} (e.g., Blandford et al. 1990). In the soft X-ray band of Seyfert 1 galaxies, broad and narrow emission lines are also observed (e.g., Costantini et al. 2007, 2016; Kaastra et al. 2000). Although in some Seyfert 2 galaxies the spatial extent of the optical and X-ray narrow emission line regions is remarkably similar (Bianchi et al. 2006), the relation of narrow emission lines in the optical and X-ray bands are not fully understood. Similarly, the connection of optical to X-ray broad emission lines is also poorly understood.

6

Optical broad emission lines are known to vary, as they are dependent on the luminosity of the nucleus (Bentz et al. 2013, and references therein). Optical narrow emission lines (e.g. [O III]) are historically thought to be constant in flux and used to calibrate spectroscopic monitoring data (Peterson et al. 2013). However, there is also a growing number of studies (Denney et al. 2014; Detmers et al. 2009; Landt et al. 2015; Peterson et al. 2013) suggesting that the optical and/or X-ray narrow emission lines in active galactic nuclei (AGN) are variable over long timescales (at least a few years). This is not totally unexpected considering the photoionization origin of these emission lines, the variable ionizing source and the distance of the narrow-line region (at least a few parsecs, Bennert et al. 2006a,b).

NGC 3783 is a nearby ($z = 0.009730$, Theureau et al. 1998) Seyfert 1 galaxy that has been extensively studied for the past few decades in the infrared, optical, UV and X-ray wavelength ranges (e.g., Chelouche & Netzer 2005; Fukumura et al. 2018; Goosmann et al. 2016; Hönig et al. 2013; Kaspi et al. 2000; Kraemer et al. 2001; Onken & Peterson 2002; Ramírez et al. 2005). NGC 3783 has a supermassive black hole with $M_{\rm BH} = (3.0 \pm 0.5) \times 10^7$ M$_\odot$ (Peterson et al. 2004). The radius of the optical broad-line region in NGC 3783 ranges from 0.0012 pc (or 1.4 light-days for He II) to 0.0086 pc (or 10.2 light-days for Hβ, Peterson et al. 2004).

On 11 and 21 December 2016, our *Swift* monitoring program[1] triggered two joint *XMM-Newton*, *NuSTAR* and Hubble Space Telescope (HST) observations targeting NGC 3783 (Mehdipour et al. 2017). This is because the soft X-ray continuum of NGC 3783 was heavily obscured (See Fig. 2 in Mehdipour et al. 2017), similar to the obscuration events discovered in NGC 5548 (Kaastra et al. 2014) and NGC 985 (Ebrero et al. 2016). The obscurer in NGC 3783 is found to partially cover the central source with a column density on the order of $10^{27}\ \mathrm{m}^{-2}$ (Mehdipour et al. 2017). The obscurer is outflowing with a range of velocities up to $6000\ \mathrm{km\ s}^{-1}$ and it is probably a disk wind at the outer broad-line region of the AGN (Mehdipour et al. 2017). Moreover, based on X-ray data accumulated in the past two decades, Kaastra et al. (2018) suggest that obscuration events with $N_{\mathrm{H}} \gtrsim 10^{26}\ \mathrm{m}^{-2}$ are a frequent phenomenon in NGC 3783.

Here we present a study of photoionized emission features in the soft X-ray band of NGC 3783 from our recent observations in December 2016 and archival observations in 2000–2001. This paper is structured as follows: In Section 6.2, we list all the observations used. Then we detail the spectral analysis in Section 6.3, including the data treatment and the model description, which has been briefly mentioned in Mehdipour et al. (2017). We present the results of our spectral analysis in Section 6.4, as well as discussions of physical implications. Conclusions are available in Section 6.5.

6

6.2. Observations and data reduction

In 2000–2001 absorption features in NGC 3783 caused by the warm absorber were clearly detectable, as well as the O VIII and C VI Lyα emission lines and the He-like triplets of O VII (Blustin et al. 2002; Kaspi et al. 2000). However, in December 2016, the soft X-ray continuum was heavily absorbed by the obscurer so that narrow absorption features caused by the warm absorber were hardly visible. Due to this diminished continuum, narrow emission features are better visible in December 2016. This includes O VII narrow radiative recombination continuum (RRC), which is a characteristic emission feature of a photoionized plasma (Liedahl & Paerels 1996).

The spectral analysis of such complicated spectra depends crucially on disen-

[1]The X-ray hardness variability of eight type-I AGN was monitored with *Swift* in 2016 in order to find intense obscuration events and thereby study them with joint Hubble Space telescope, *XMM-Newton*, and *NuSTAR* observations (Mehdipour et al. 2017).

tangling the true continuum from the effects of the obscuration and absorption features, which may include many lines and edges that are unresolved and overlapping, as well as emission features. That is to say, this requires a model capable of fitting essentially the overall continuum as well as all the absorption and emission features, including those that cannot be clearly resolved.

Therefore, as described in Mehdipour et al. (2017), we construct a time-averaged spectrum in 2000 and 2001 to constrain the intrinsic spectral energy distribution (SED) and emission features in the unobscured state. Archival data from the optical monitor (OM, Mason et al. 2001), Reflection Grating Spectrometer (RGS, den Herder et al. 2001), and European Photon Imaging Camera-pn (EPIC-pn, Strüder et al. 2001) from *XMM-Newton* are used. We also use archival *Chandra* High-Energy Transmission Grating Spectrometer (HETGS, Canizares et al. 2005) data in 2000, 2001 and 2013 to better constrain the photoionized absorption features, which are rather stable over the 12-year period (Scott et al. 2014). The time-averaged spectrum has a total exposure of 1.37 Ms, with 1.05 Ms for *Chandra*/HETGS and 324 ks for *XMM-Newton*/RGS , respectively.

The optical to hard X-ray data in December 2016 are used for determining the intrinsic SED, obscuration effect, and photoionized emission features (present work) in the obscured state. The two data sets in December 2016 are fitted independently as the continua are different (e.g. Figure 2 in Mehdipour et al. 2017).

All the data used for the present work are listed in Table 6.1. The exposures of the obscured *XMM-Newton*/RGS spectra are 110 ks and 56 ks, respectively. A detailed description of the data reduction can be found in Appendix A of Mehdipour et al. (2015, for NGC 5548), which also applies to the NGC 3783 data used here.

6.3. Spectral analysis

The spectral analysis package SPEX (Kaastra et al. 1996) v3.04 is used, incorporating state-of-the-art atomic data, including radiative recombination (Badnell 2006; Mao & Kaastra 2016) and electron energy loss due to radiative recombination (Mao et al. 2017a). We use C-statistics following Kaastra (2017) throughout this work. Statistical errors are quoted at 68.3% (1σ) confidence level ($\Delta C = 1.0$) unless indicated otherwise. X-ray spectra are optimally binned according to Kaastra & Bleeker (2016). Spectra shown in this paper are background subtracted and displayed in the observed frame.

Table 6.1: List of NGC 3783 data used for the present spectral analysis.

Observatory	Inst.	ObsID	Start date	Length
Chandra	ACIS/HETG	373	2000-01-20	56 ks
XMM-Newton	OM, RGS, pn	0112210101	2000-12-28	40 ks
Chandra	ACIS/HETG	2090	2001-02-24	166 ks
Chandra	ACIS/HETG	2091	2001-02-27	169 ks
Chandra	ACIS/HETG	2092	2001-03-10	165 ks
Chandra	ACIS/HETG	2093	2001-03-31	166 ks
Chandra	ACIS/HETG	2094	2001-06-26	166 ks
XMM-Newton	OM, RGS, pn	0112210201/0401	2001-12-17	142 ks
XMM-Newton	OM, RGS, pn	0112210501/0601	2001-12-19	142 ks
Chandra	ACIS/HETG	14991	2013-03-25	59 ks
Chandra	ACIS/HETG	15626	2013-03-27	102 ks
HST	COS	LD3E03	2016-12-12	2 orbits
XMM-Newton	OM, RGS, pn	0780860901	2016-12-11	110 ks
NuSTAR	FPMA, FPMB	80202006002	2016-12-11	56 ks
HST	COS	LD3E04	2016-12-21	2 orbits
XMM-Newton	OM, RGS, pn	0780861001	2016-12-21	56 ks
NuSTAR	FPMA, FPMB	80202006004	2016-12-21	46 ks

6.3.1. Optical to X-ray spectra construction

The unobscured (2000–2001) and obscured (December 2016) spectra are constructed with all available data in each epoch as follows:

1. OM flux at V, B, U, UVW1, UVM2, and UVW2 bands;

2. Cosmic Origins Spectrograph (COS, Green et al. 2012) flux at 1139 Å, 1339 Å, 1477 Å, and 1794 Å, free from emission and absorption features;

3. first-order RGS data (RGS1 and RGS2 combined) in the $7-37$ Å wavelength range, in order to better constrain the emission and absorption features especially for $\lambda \gtrsim 25$ Å;

4. first-order MEG (Medium Energy Grating) data (positive and negative orders combined) in the $6-17$ Å wavelength range, which have better energy resolution compared to the RGS data at the same wavelength range. Note that MEG data are broken into several segments, with the local continuum of each segment re-scaled by $\lesssim \pm 15$ % to match the RGS continuum at the same wavelength range. The scaling factor of each segment is 1.158 for 6–7 Å, 1.120 for 7–8 Å, 1.003 for 8–9 Å, 1.029 for 9–11 Å, 0.889 for 11–14 Å, and 0.850 for 14–17 Å, respectively. This is to account for observations taken at different epochs, as well as the cross calibration between RGS and MEG;

5. first-order HEG (High Energy Grating) data (positive and negative orders combined) in the $1.7-3$ Å wavelength range, which has better energy resolution compared to the pn data in the same wavelength range. The HEG data are re-scaled by a factor of 1.218;

6. EPIC-pn data in the $1.5-10$ keV energy range (i.e. the 1.24–8 Å wavelength range). EPIC-pn data are re-scaled by 1.038 (2000–2001);

7. *NuSTAR* data in the $10-78$ keV energy range. *NuSTAR* data are re-scaled by 1.013 (11 December 2016) and 1.027 (21 December 2016), respectively.

The above optical to X-ray data are fitted simultaneously, which allows us to constrain the broadband (optical, UV and X-ray) continuum and the X-ray obscuration, absorption and emission features at the same time. Note that the COS grating spectra are analyzed in a separate paper (Kriss et al. in prep.).

6

6.3.2. Description of model components

In order to interpret the continuum, absorption and emission part of the spectrum at the same time, the following model components needs to be taken into account:

1. The intrinsic broadband spectral energy distribution (SED) of the AGN.
2. The obscuration effect caused by the obscurer and the high-ionization component in the obscured state.
3. Absorption features caused by the warm absorber.
4. Broad and narrow emission features caused by the X-ray photoionized emitter.
5. Broad and narrow emission lines in the optical/UV.
6. The host galaxy continuum emission in the optical/UV.
7. The Galactic extinction in the optical/UV and absorption in X-rays.

We refer readers to Mehdipour et al. (2017) for details of model components 2, 5, 6 and 7. The protosolar abundances of Lodders & Palme (2009) are used for all plasma models.

6.3.2.1. Intrinsic broadband SED of the AGN

A photoionization continuum is required for photoionization modeling of the obscurer, warm absorber, and X-ray photoionized emitter. Following previous analysis of NGC 5548 (Mehdipour et al. 2015), we fit the optical to X-ray data of NGC 3783 using a model consisting of a Comptonized disk component (COMT, Titarchuk 1994) for optical to soft X-rays, a power-law component (POW), and a neutral reflection component (REFL, Magdziarz & Zdziarski 1995; Zycki et al. 1999) for hard X-rays. An exponential cut-off is applied to the high- and low-energy end of the power-law component (Appendix 6.A). The intrinsic optical to X-ray continuum and all the obscuration, absorption, emission, and extinction effects are fitted simultaneously. Therefore, the fit iterates many times to get the best-fit intrinsic broadband SED of the AGN (results in Section 6.4.1).

6.3.2.2. Photoionization continuum

A photoionization continuum is required for the photoionization modeling and it can be different from the AGN SED mentioned above. The photoionization continuum received by the obscurer is indeed simply the contemporary AGN SED (Table 6.2).

For the warm absorber, in 2000–2001, when NGC 3783 is not obscured, its photoionization continuum is also the contemporary AGN SED. However in December 2016 the photoionization continuum for the warm absorber is the contemporary AGN SED with the obscuration effect taken into account.

The photoionization continuum received by the X-ray narrow-line region is assumed to be the 2000–2001 (time-averaged) AGN SED for all epochs (2000–2001 and December 2016). This is because if the photoionized plasma is too far away from the nucleus and/or the density of the plasma is too low, the plasma is in a quasi-steady state with its ionization balance varying slightly around the mean value corresponding to the mean ionizing flux level over time (Kaastra et al. 2012; Nicastro et al. 1999; Silva et al. 2016). Note that our assumption implies that the obscurer does not subtend a large solid angle so that it barely screens photons from the nucleus to the X-ray narrow emission component or the screened photons have not arrived the X-ray narrow emission component yet.

On the other hand, the photoionization continuum for the X-ray broad-line region is the intrinsic SED of NGC 3783. The density of the broad-line region is in general orders of magnitude higher than that of the narrow-line region, thus, the broad-line region responds much faster to changes in the photoionization continuum. No obscuration effect is taken into account for all epochs (2000–2001 and December 2016), since the obscurer is likely farther away than the broad-line region (Mehdipour et al. 2017). In Section 6.4.3, we show results of our independent check on this assumption.

6

6.3.2.3. Warm absorber

We use the photoionization plasma model PION in SPEX to account for the absorption features produced by the warm absorber. As described in Section 6.4.2, we require nine PION absorption components. For the time-averaged unobscured spectrum (2000–2013), we allow hydrogen column densities ($N_{\rm H}$), ionization parameters ($\log \xi$), and outflow velocities ($v_{\rm out}$) free to vary. After a few trials, microscopic turbulence velocities[2] ($v_{\rm mic}$) are coupled for components 1–2, 3–7, and 8–9 to reduce unnecessary free parameters. For the obscured spectra (December 2016), all the above parameters are fixed to values obtained in the unobscured spectrum, except the ionization parameters, which are assumed to be proportional to the $1 - 10^3$ Ryd ionizing luminosity. That is to say, the hydrogen number den-

[2]The Doppler parameter $b = (v_{\rm th}^2 + 2v_{\rm mic}^2)^{1/2}$, where $v_{\rm th} = \sqrt{2kT/m}$ is the thermal broadening velocity, T the temperature, and m the atomic mass. The full width at half maximum $\mathrm{FWHM} = 2\sqrt{\ln\ 2}\ b$. In the PION model in SPEX, $v_{\rm mic}$ is the "v" parameter.

sity times distance squared ($n_{\rm H} r^2$) of the warm absorber in the obscured state is assumed to be the same as in the unobscured state. In both unobscured and obscured states, for each PION absorption component, the absorption ($C_{\rm abs} = 1$) and emission ($C_{\rm em} = 0$) covering factors are fixed[3]. That is to say, we assume that the warm absorber fully covers the line of sight but has negligible extent with respect to the nucleus.

6.3.2.4. X-ray photoionized emitter

Similar to the previous analysis on NGC 5548 (Mao et al. 2018), the narrow emission features in NGC 3783 can be reasonably fitted with two PION components (details in Section 6.4.3). Whether the soft X-ray continuum is obscured or not, four free parameters of each PION emission component are allowed to vary, namely $N_{\rm H}$, $\log \xi$, $v_{\rm mic}$ and $C_{\rm em}$. Since the emission lines are consistent with not outflowing, as shown by previous studies (Behar et al. 2003; Kaspi et al. 2002), the outflow velocity ($v_{\rm out}$) is fixed to zero for each PION emission component. In addition, for each PION emission component, its absorption covering factor $C_{\rm abs}$ is fixed to zero.

Broad emission features are modeled with a third PION component. For the time-averaged unobscured spectrum (2000–2001), where the *XMM-Newton* and *Chandra* grating spectra are fitted simultaneously, four free parameters of this PION emission component are allowed to vary, including $N_{\rm H}$, $\log \xi$, $v_{\rm mic}$ and $C_{\rm em}$. For the obscured spectra (December 2016), these parameters are fixed to values obtained in the unobscured spectrum, except the ionization parameters, which are assumed to be proportional to the $1 - 10^3$ Ryd ionizing luminosity (Table 6.2).

For simplicity, all three emission components are assumed to be free of further absorption by the warm absorber (see discussion in Section 6.4.5).

6.4. Results and discussions

6.4.1. Intrinsic broadband SED of the AGN

The time-averaged intrinsic SED of NGC 3783 in 2000-2013 is shown in Figure 6.1. The intrinsic SED on 11 December 2016 is also shown for comparison, which is similar to that on 21 December 2016. Fig. 6 of Mehdipour et al. (2017) presents a version with the intrinsic SEDs overplotted with the observational data. The corresponding best-fit continuum parameters are listed in Table 6.2.

The two observations in December 2016 have similar intrinsic SEDs. However,

[3]In the PION model in SPEX, $C_{\rm abs}$ and $C_{\rm em}$ are the "fcov" and "omeg" parameters.

6

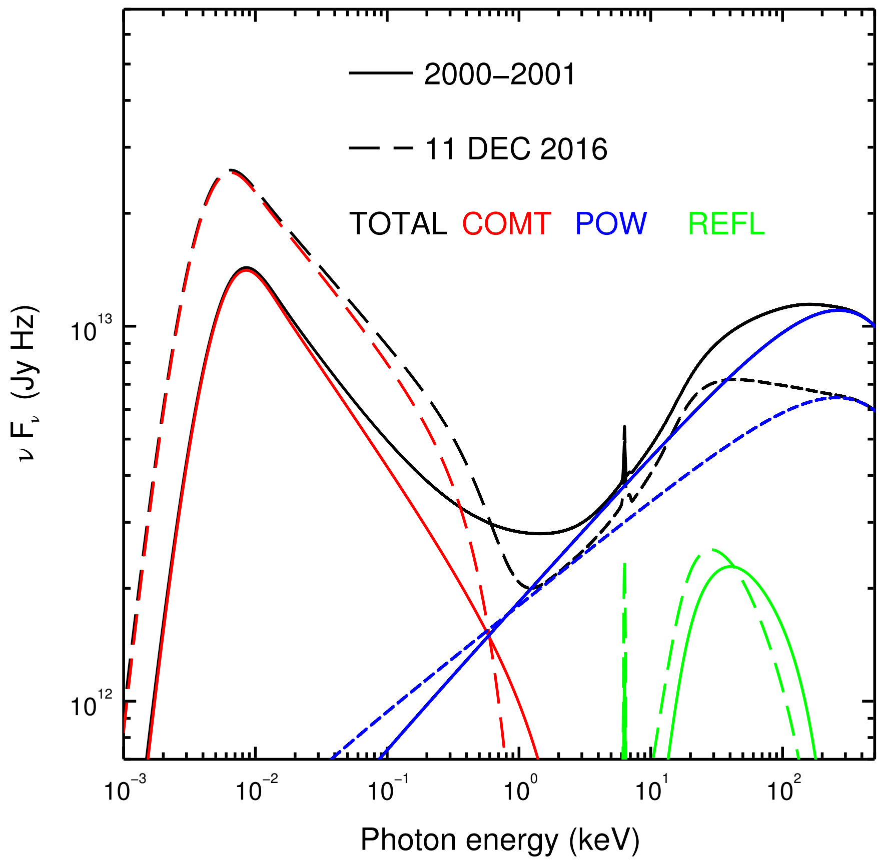

Figure 6.1: The intrinsic spectral energy distribution of NGC 3783 for the time-averaged data in 2000–2001 (solid lines) and 11 December 2016 data (dashed lines). Contributions from individual components are shown in red for the Comptonized disk component (COMT), blue for the power-law component (POW) and green for the reflection component (REFL).

Table 6.2: Best-fit parameters of the intrinsic broadband SED of NGC 3783 in 2000-2001 and December 2016.

Date	2000-2001	11 DEC 2016	21 DEC 2016
	COMT		
Norm	0.95 ± 0.05	9.7 ± 0.3	10.3 ± 0.4
$T_{\rm seed}$	1.47 ± 0.05	1.08 ± 0.03	1.08 ± 0.02
$T_{\rm c}$	0.54 ± 0.02	0.13 ± 0.02	0.14 ± 0.03
τ	9.9 ± 0.2	22.0 (f)	22.0 (f)
	POW		
Norm	2.40 ± 0.03	2.42 ± 0.16	3.03 ± 0.19
Γ	1.61 ± 0.01	1.73 ± 0.02	1.75 ± 0.02
C-stat / C-expt.	6092 / 2563	2335 / 1552	2340 / 1555
$L_{0.3-2\ \rm keV}$	1.20	1.28	1.52
$L_{2-10\ \rm keV}$	1.16	0.94	1.11
$L_{0.001-10\ \rm keV}$	10.6	18.8	21.1
$L_{1-1000\ \rm Ryd}$	7.01	10.2	11.9

Notes. Parameters followed by (f) are fixed in the fit. The temperature of seed photons is in units of eV, the warm corona temperature in keV, the normalization of the warm comptonization (COMT) component in 10^{55} ph s^{-1} keV^{-1}, and the normalization of the power-law (POW) component in 10^{51} ph s^{-1} keV^{-1} at 1 keV. The C-stat refer to the final best-fit, where all obscuration, absorption, emission and extinction effects are taken into account. The luminosities of COMT plus POW in different energy ranges are in units of 10^{36} W with uncertainties about $3-5\%$.

for the time-averaged SED in 2000–2013, both the Comptonized disk component and the power-law component differ significantly from December 2016.

We should emphasize that we apply a global SED model to fit the optical to hard X-ray data, thus, the continuum model in the present work differs from previous studies. Kaspi et al. (2001) and Scott et al. (2014) fitted the 1–26 Å continuum with "line-free zones" (LFZs). However, as pointed out by Scott et al. (2014), even when LFZs are entirely line-free, absorption edges still contribute to curvature in the spectrum. The 0.5–10 keV continuum of NGC 3783 has also been fitted by a power law with $\Gamma \in (1.5,\ 1.83)$ (Blustin et al. 2002; De Rosa et al. 2002), sometimes including an extra thermal component with $kT \sim 0.1$ keV (Krongold et al. 2003). Fu et al. (2017) constructed a SED with typical AGN SED (Elvis et al. 1994) but scaled with wavelength ($\propto \lambda^{-0.27}$) to match the intrinsic UV $(1135 - 1795$ Å) and X-ray $(2 - 11$ Å) continuum.

6.4.2. Warm absorber

6

The best-fit C-stat to expected C-stat ratio for the time-averaged spectrum in 2000–2013 is $6092/2563 \gtrsim 2$ (with 2505 degrees of freedom), which is not statistically acceptable. This is due to the very high photon statistics compared with systematic uncertainties in the instrumental response, the imperfect cross calibration of different instruments, and our model is still rather simple compared to the reality. But the result is still useful to assess whether the observed continuum and all absorption (and emission) features are reasonably accounted for. The best-fit time-averaged (2000, 2001 and 2013) MEG spectrum (6–15 Å) is shown in details in Figure 6.2. The best-fit time-averaged (2000–2001) RGS spectrum (8–35 Å) is fitted simultaneously but shown separately in Figure 6.3 for clarity.

There are in total nine PION absorption components for the warm absorber, with components 1–4 dominating highly ionized ions with large atomic number (e.g. Fe XXVI, Fe XVII, and Si XIV), components 5 and 6 mainly accounting for moderately ionized ions with intermediate atomic number (e.g. Mg IX, O VIII and O V), and components 7–9 for lowly ionized ions with intermediate atomic number (e.g. N IV and C IV). Contributions from individual warm absorber components (in percentage) to ions with column density $N_{\rm ion} \gtrsim 10^{20}~{\rm m}^{-2}$ are shown in Figure 6.4. Components 7–9 are required in our model because we include the RGS spectrum above 25 Å, while previous analyses simply focus on spectra at shorter wavelength range with $\lambda \lesssim 25$ (Behar et al. 2003; Krongold et al. 2003, for RGS and MEG, respectively). Admittedly, the signal-to-noise ratio decreases toward the longer wavelength, thus,

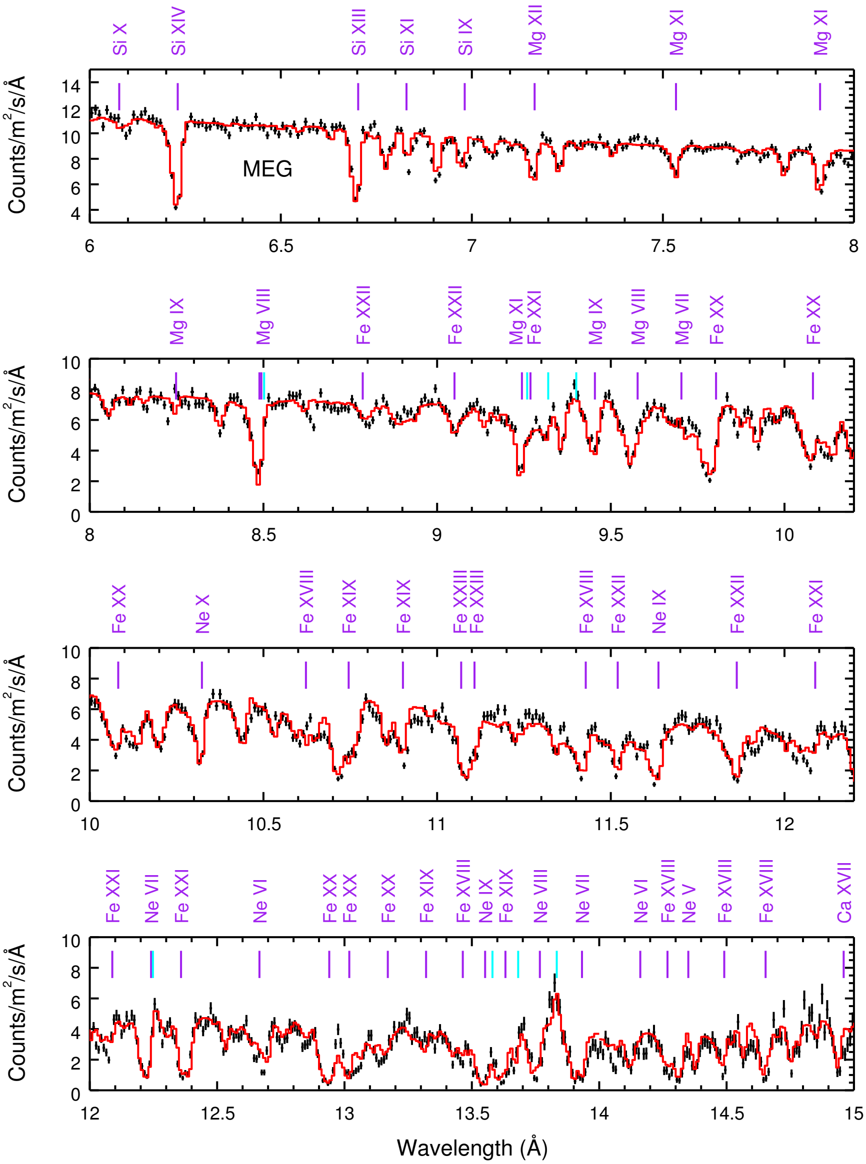

Figure 6.2: The best-fit to the time-averaged MEG spectrum (in the observed frame) of NGC 3783 observed in 2000, 2001 and 2013. Most prominent absorption and emission features are labeled. The solid vertical lines in purple (blue) indicate the photoionized absorption (emission) features.

6

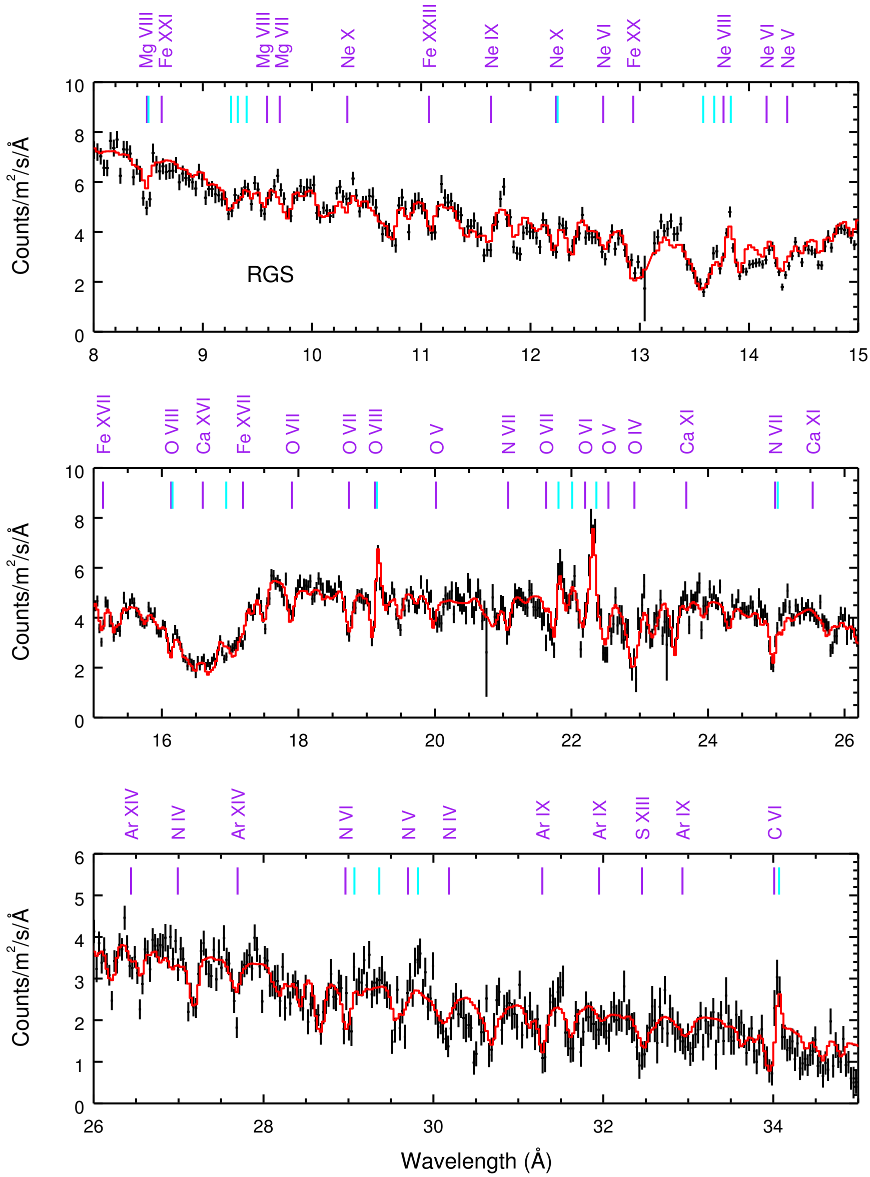

Figure 6.3: Similar to Figure 6.2 but for the time-averaged RGS spectrum (in the observed frame) of NGC 3783 observed in 2000 and 2001.

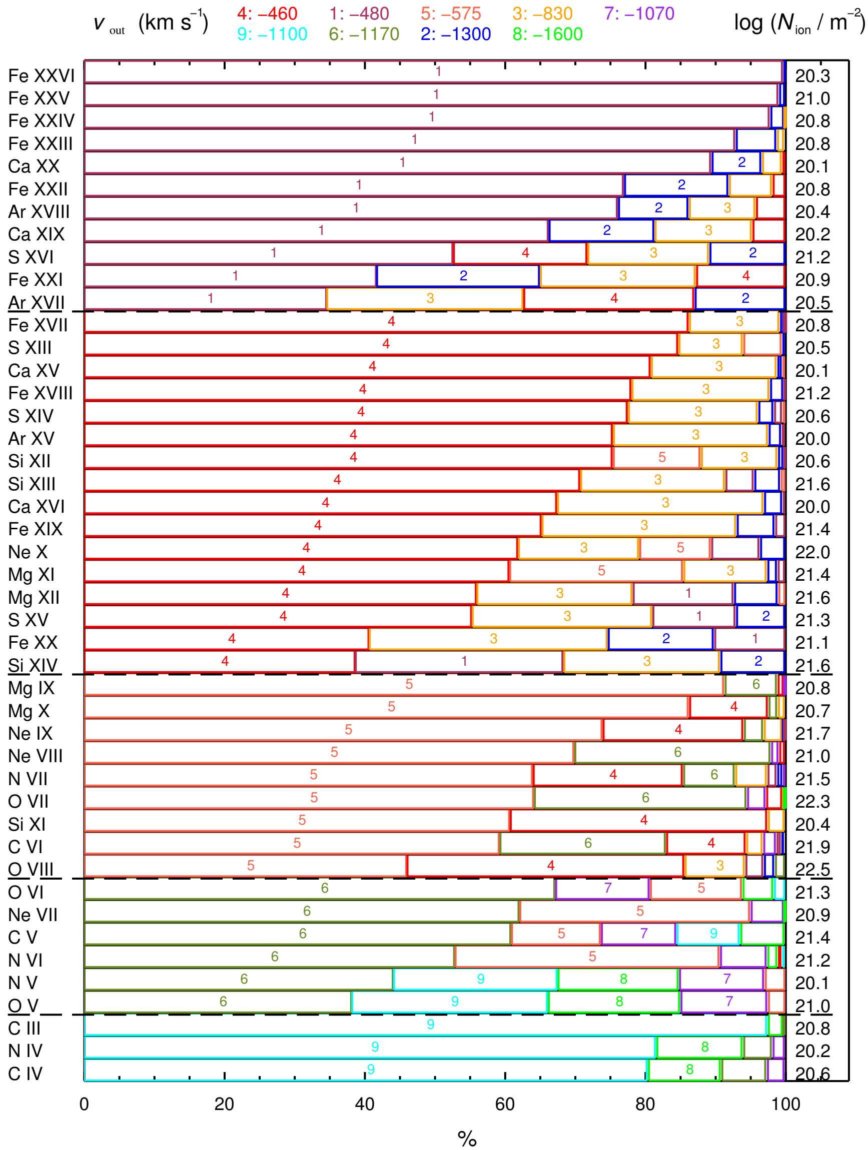

Figure 6.4: Ionic column density (units: m^{-2}, in log-scale listed to the right) with contributions from individual warm absorber components (in percentage). Ions with $N_{\mathrm{ion}} \gtrsim 10^{20}\ \mathrm{m}^{-2}$ are listed to the left. The warm absorber components are color coded with outflow velocities (v_{out}) listed to the top. The ionization parameters of the warm absorber components increase from component 9 to component 1.

Table 6.3: Best-fit parameters of the warm absorber components in the time-averaged spectra of NGC 3783 in 2000–2013.

Comp.	$N_{\rm H}$ 10^{25} m^{-2}	$\log_{10}(\xi)$ 10^{-9} W m	$v_{\rm mic}$ km s^{-1}	$v_{\rm out}$ km s^{-1}
1	11.1 ± 0.8	3.02 ± 0.01	120 ± 10	-480 ± 10
2	2.1 ± 0.2	2.74 ± 0.03	120 (c)	-1300 ± 25
3	6.1 ± 0.6	2.55 ± 0.02	46 ± 2	-830 ± 15
4	12.4 ± 0.5	2.40 ± 0.01	46 (c)	-460 ± 10
5	5.0 ± 0.2	1.65 ± 0.01	46 (c)	-575 ± 10
6	1.2 ± 0.2	0.92 ± 0.04	46 (c)	-1170 ± 30
7	$0.15^{+0.05}_{-0.14}$	$0.58^{+0.28}_{-0.17}$	46 (c)	-1070 ± 40
8	$0.07^{+0.15}_{-0.01}$	$-0.01^{+1.82}_{-0.05}$	790 ± 100	-1600 ± 800
9	0.44 ± 0.03	-0.65 ± 0.06	790 (c)	-1100 ± 140

Notes. Microscopic turbulence velocities ($v_{\rm mic}$) followed by (c) are coupled to $v_{\rm mic}$ of another component with the same value in the fit.

6

the best-fit parameters of components 7–9 are less well constrained. All the best-fit parameters for the warm absorber components of NGC 3783 in the 2000–2013 time-averaged spectra are tabulated in Table 6.3.

The hydrogen column density ($N_{\rm H}$) of the warm absorber is dominated by components 1–6 with $N_{\rm H}^{\rm total} \simeq 3.8 \times 10^{26}$ m^{-2}, similar to previous results by Netzer et al. (2003) with $N_{\rm H}^{\rm total} \sim 4 \times 10^{26}$ m^{-2}, which is higher than $N_{\rm H}^{\rm total} \sim 2 - 3 \times 10^{26}$ m^{-2} found by Kaspi et al. (2002) and Krongold et al. (2003).

Since the photoionization continuum, abundance table and number of absorption components used by different authors are different, we do not compare the ionization parameters with previous results (e.g., Kaspi et al. 2002; Krongold et al. 2003; Netzer et al. 2003).

In the present work, the microscopic turbulence velocities of the absorption components are 50 km s^{-1} for Components 3–7, 120 km s^{-1} for Components 1–2, and 800 km s^{-1} for Components 8 and 9, respectively (Table 6.3). The microscopic turbulence velocity found in the literature also cover a wide range of values, with ~ 100 km s^{-1} for Kaspi et al. (2000) and Behar et al. (2003), ~ 200 km s^{-1} for Krongold et al. (2003); Netzer et al. (2003), and up to $400 - 600$ km s^{-1} for a few ions in Table 3 of Kaspi et al. (2002).

Our best-fit outflow velocities vary for different absorption components, ranging from -450 km s^{-1} to -1300 km s^{-1}. A wide range of outflow velocities are also reported in the literature, including -300 to -1000 km s^{-1} by Kaspi et al. (2002), -470 to -800 km s^{-1} by Behar et al. (2003), -750 km s^{-1} by Krongold et al. (2003), and -400 to -1300 km s^{-1} by Netzer et al. (2003).

We also note that the PION model in the SPEX code takes advantage of recently updated atomic data, which is more accurate and complete than previous models by Krongold et al. (K03, 2003) and Netzer et al. (N03, 2003). Previous models are able to fit some of the strong absorption lines but insufficient to fit the global spectrum. As pointed out by Netzer et al. (2003), the K03 model provides a better fit to the Fe UTA (unresolved transition array) yet fails to fit the Si X and Si XI lines around 6.8 Å. The N03 model has a better fit over the 5–7 Å wavelength range while the UTA features are poorly fitted. As for the PION model, we refer readers to Section 4.29 of the SPEX manual for a detailed model description, Mehdipour et al. (2016) for a comparison with other popular photoionization codes and Mao et al. (2017b) for a list of characteristic ground and metastable absorption lines.

6.4.3. X-ray photoionized emitter

6

In our PION modeling of the emission features (lines and RRCs), we find that a broad emission component is required in addition to two narrow emission components. For the time-averaged spectrum, the best-fit with only narrow emission components yields a C-stat of 6301 (d.o.f. = 2508), while the best-fit with both broad and narrow emission components yields a C-stat of 6092 (d.o.f. = 2505). The broad emission component improves the fit, at least significantly in statistics ($\Delta C \sim -200$). However, regardless of the presence of the broad emission component, there are still some structures in the residuals of the above two fits (Figure 6.5). Future missions (e.g., *Arcus*, Smith et al. 2016) with adequate spectral resolution and significantly larger photon collecting area are essential to verify the presence of such broad emission features in X-rays.

The broad emission component is obtained via convolving a narrow ($v_{\rm mic}$ = 100 km s^{-1}) PION component with a velocity broadening model (VGAU in SPEX) with a fixed σ_v, so that the broadening effect applies to both emission lines and RRCs. Such kind of broadening is probably due to the macroscopic motion of the emitter. Unfortunately, the velocity broadening in X-rays is a difficult parameter to determine. It cannot be too narrow, otherwise there is no significant improvement on the C-stat. It cannot be too broad either, otherwise it is unclear whether we are fitting the broad emission line or a part of the complex continuum. At this stage, we tentatively fixed the value of σ_v ($= v_{\rm mac}$) to 9000 km s^{-1}. This value is within

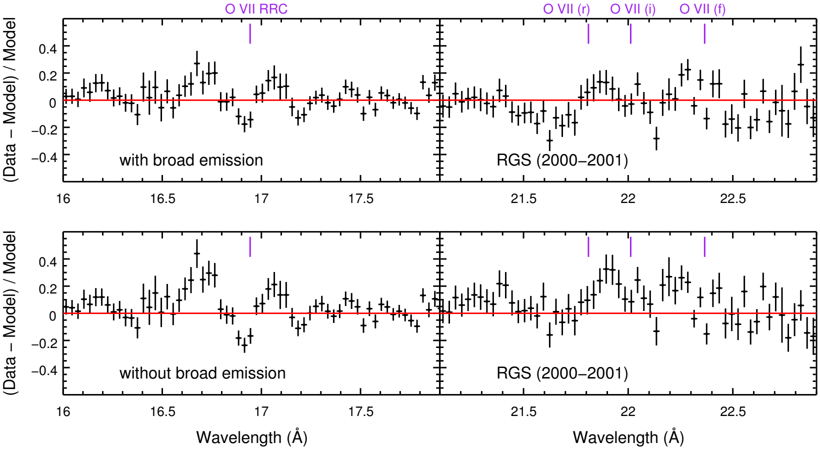

Figure 6.5: Residuals of the best-fit to the time-averaged RGS spectrum (in the observed frame) of NGC 3783 in 2000–2001 around the O VII RRC (left panels) and O VII He-like triplets (right panels). The upper and lower panels show residuals of the best-fit with and without the broad (FWHM∼ $21000\ \mathrm{km\ s^{-1}}$) PION emission component (the third component in Table 6.4), respectively.

the range of typical gas velocity $3000 - 10000\ \mathrm{km\ s^{-1}}$ (Blandford et al. 1990) in the broad line region. For NGC 3783, the X-ray velocity broadening corresponds to a full width at half maximum (FWHM $= 2.355\ \sigma_v$) of about $21000\ \mathrm{km\ s^{-1}}$, which is significantly larger than FWHM(Hβ) $\sim 3000\ \ \mathrm{km\ s^{-1}}$ (Onken & Peterson 2002) in optical, but close to the width of the broadest component of Lyα in the UV, FWHM∼18000$\mathrm{km\ s^{-1}}$ (Kriss et al., in prep.).

The broad and narrow emission model components derived from the 2000–2001 data do not match the data observed in December 2016 (the orange line in Figure 6.6). Narrow emission features might have varied slightly over the 15-year timescale (Section 6.4.4). The broad emission component seems to be much weaker in December 2016 (Figure 6.6). This apparent weakening can be accounted for by applying the obscuration to the broad emission component (the purple line in Figure 6.6). The parameters for the obscurer used here are the same as given in Table 1 of Mehdipour et al. (2017). The above interpretation supports the picture suggested by Mehdipour et al. (2017) that the obscurer is currently at the outer broad-line region of the AGN.

The best-fit to the RGS spectrum on 11 December 2016 is shown in Figure 6.7, which is similar to that on 21 December 2016. The best-fit parameters of the X-ray photoionized emitter in 2000–2001 and December 2016 are listed in Table 6.4. While the emission measures (E.M.$= n_e\ n_{\mathrm{H}}\ 4\pi\ C_{\mathrm{em}}\ r^2\ N_{\mathrm{H}}/n_{\mathrm{H}}$) of component 1 are

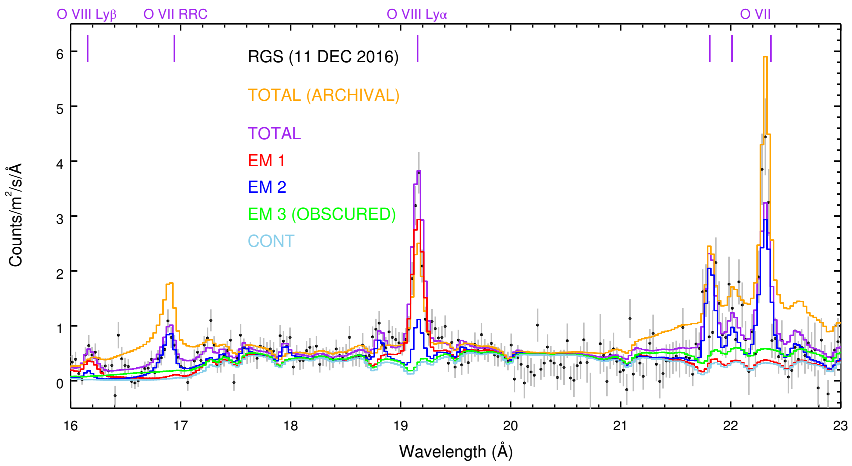

Figure 6.6: Best-fit to the $17-24$ Å RGS spectrum (in the observed frame) of NGC 3783 from 11 December 2016. The best-fit model with contributions from all emission components is shown in purple. Contributions from individual emission components are shown in different colors, with red and blue for narrow emission features and green for broad emission features. The orange solid line is a calculation using the best-fit parameters obtained from the time-averaged archival spectrum for all three emission components. Due to the obscuration effect, the broad emission component (EM 3) appears to be weaker in December 2016.

consistent (at 1σ confidence level) between epochs, the emission covering factor ($C_{\rm em}$), thus the emission measure of component 2 is an order of magnitude higher. If we fix $C_{\rm em}(\rm EM\ 2) = 0.6$ when fitting the 11 December 2016 spectrum, the best-fit C-stat is 2406, which is a worse fit ($\Delta C \sim +70$) when compared to the best-fit C-stat in Table 6.2. This might suggest an increase of the physical size of the emitter over 15 years.

Different values of the best-fit parameters of the narrow emission components in different epochs (Table 6.4) need to be interpreted with caution. Due to lack of information, we assume the photoionization continuum to be the 2000–2001 AGN SED for all spectra in 2000-2001 and December 2016. Under this assumption, the ionization parameter $\xi = L/(n_{\rm H}\ r^2)$ should be the same, because the number density ($n_{\rm H}$) and distance (r) of the emission region are not expected to vary dramatically. The column density ($N_{\rm H}$), microscopic turbulence velocity ($v_{\rm mic}$) and emission covering fraction ($C_{\rm em}$) might not vary significantly as well. Deviation from the time-average photoionization continuum can be partly due to long-term variation in the intrinsic SED components and/or the obscuration events, which might be more frequent than previously thought for NGC 3783. Based on the hardness ratio

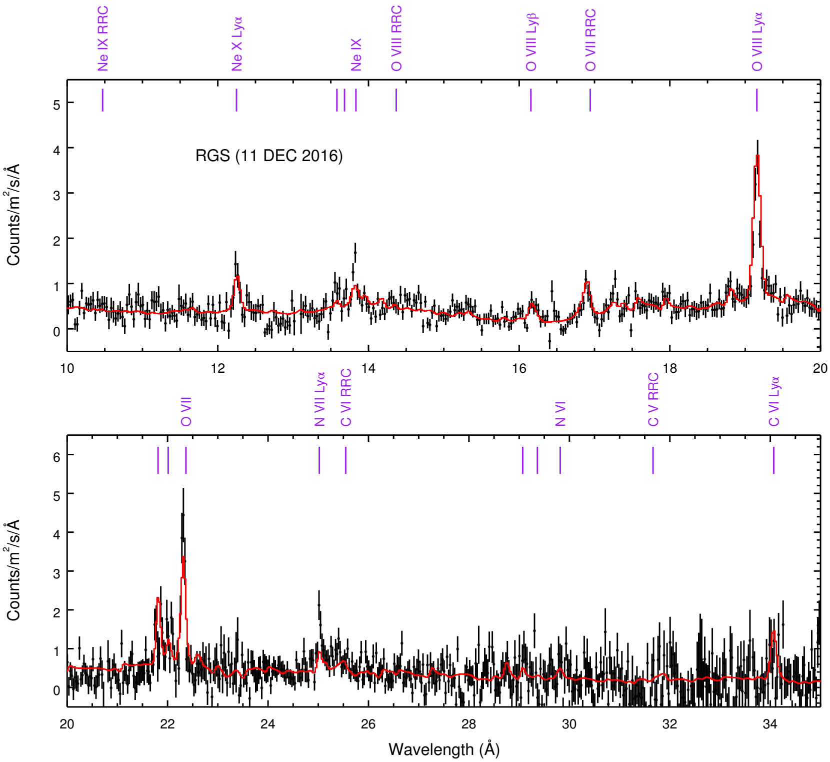

Figure 6.7: The best-fit to the RGS spectrum (in the observed frame) of NGC 3783 on 11 DEC 2016. Most prominent emission features are labeled.

Table 6.4: Best-fit results of the X-ray photoionized emitter in the time-averaged spectra of NGC 3783. The emission measure (E.M.) is calculated based on the best-fit parameters.

Comp.	$N_{\rm H}$ 10^{26} m^{-2}	$\log_{10}(\xi)$ 10^{-9} W m	$v_{\rm mic}$ km s^{-1}	$C_{\rm em}$ %	E.M. 10^{70} m^{-3}
			2000–2001		
1	60 ± 37	2.60 ± 0.07	600 ± 100	0.29 ± 0.12	$0.5^{+0.8}_{-0.4}$
2	$5.2^{+5.4}_{-2.3}$	1.35 ± 0.05	140^{+50}_{-100}	$0.6^{+0.4}_{-0.2}$	$1.5^{+4.1}_{-1.0}$
3	28^{+72}_{-5}	0.82 ± 0.02	100 (f)	$0.3^{+0.1}_{-0.2}$	13^{+53}_{-10}
			11 DEC 2016		
1	25 ± 6	2.58 ± 0.05	590 ± 90	0.98 ± 0.13	$1.0^{+0.6}_{-0.4}$
2	3.0 ± 0.7	1.03 ± 0.05	350 ± 70	7.0 ± 1.3	30^{+19}_{-13}
3	28 (f)	1.00 (f)	100 (f)	0.3 (f)	13 (f)
			21 DEC 2016		
1	35 ± 17	2.58 ± 0.05	460 ± 130	0.7 ± 0.3	$1.6^{+1.6}_{-0.9}$
2	2.3 ± 1.0	1.03 ± 0.05	270 ± 110	7.3 ± 2.4	28^{+32}_{-19}
3	28 (f)	1.06 (f)	100 (f)	0.3 (f)	13 (f)

Notes. Parameters followed by (f) are fixed in the fit. The 2000–2013 MEG ($6-17$ Å) data and the 2000–2001 RGS ($7-37$ Å) data are fitted simultaneously (Section 6.3.1), but constraints are obtained mainly from the 2000–2001 RGS data since it covers all the emission features from Ne, O, N, and C.

of all *Swift*/XRT spectra in 2008–2017, obscuration events might occur about half of the time (Kaastra et al. 2018), which will affect the photoionization modelling of the X-ray narrow emission features.

Additionally, by comparing the best-fit results of the absorption (Table 6.3) and emission (Table 6.4) components, we find that emission component 1 and absorption component 3 share similar ionization parameter, yet the hydrogen column density, turbulence velocity and outflow velocity are significantly different. The ionization parameter of emission component 2 has no counterpart in absorption components. This is similar to what we find in another Seyfert 1 galaxy NGC 5548 (Mao et al. 2018). It is possible that the X-ray emission and absorption components are not related, although we need distance (thus density) measurement on these components to verify this deduction.

6.4.4. Variability of the X-ray emission features

We check the variability of the most prominent narrow emission lines, the O VIII Lyα line and O VII He-like triplets, in the RGS spectra in 2000–2001 and December 2016. A phenomenological local fit is used in this exercise so that we are not confused by the unknown photoionization continuum effect on the photoionization modeling.

We fix the continuum to the best-fit global continuum corrected for the foreground Galactic absorption, the obscurer, the warm absorber and the broad emission features. Subsequently, the narrow emission lines are accounted for with Gaussian line profiles. The normalization and velocity broadening of the Gaussian profiles are free to vary, except that we limit the velocity broadening to be no larger than $2000~\mathrm{km~s^{-1}}$ and couple the broadening of the resonance and intercombination lines of the O VII He-like triplets. The line luminosity and velocity broadening are listed in Table 6.5. The best-fit results of 2000–2001 and 11 December 2016 are plotted in Figs. 6.8 and 6.9.

These emission lines are consistent with each other at a 1σ confidence level between the two observations in December 2016. When compared to 2000–2001, the O VII resonance and forbidden lines remain constant in luminosity at the 1σ confidence level, while the O VIII Lyα line and intercombination line of He-like O VII are marginally brighter in December 2016 at the 2σ confidence level. In addition, the resonance and intercombination lines of O VII appear to be broader in December 2016, although the uncertainty is large.

Since the variability of the X-ray broad emission features cannot be checked directly, we turn to the very broad (FWHM$\gtrsim 10^4~\mathrm{km~s^{-1}}$) emission lines in the high-

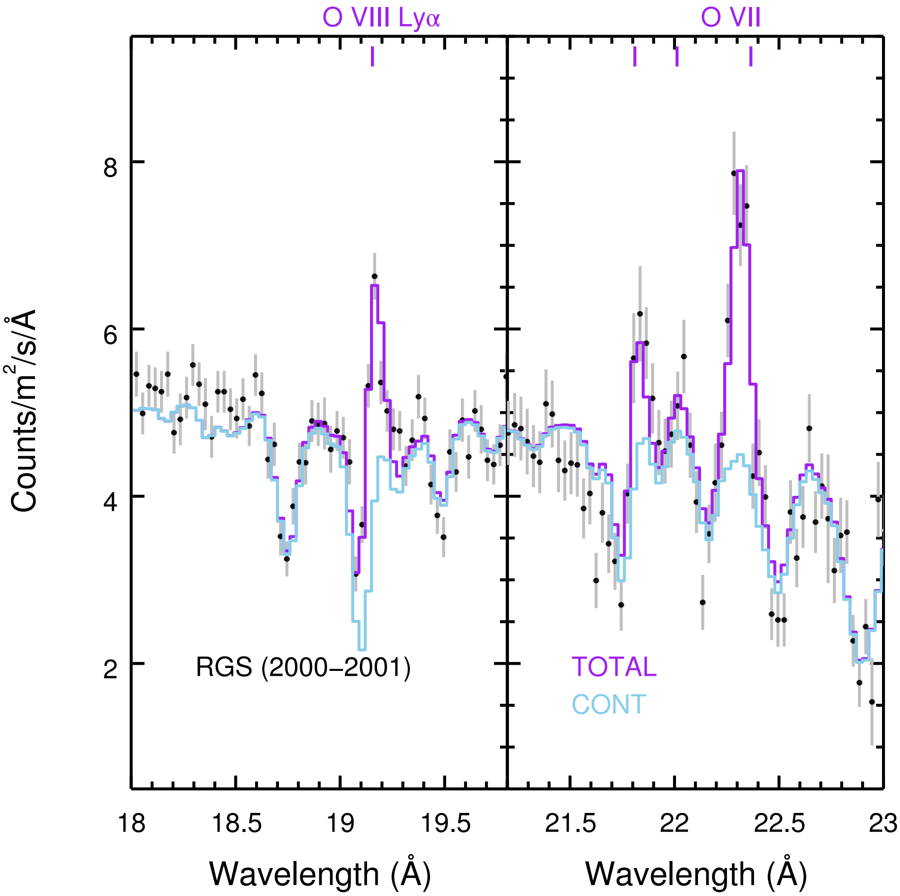

Figure 6.8: Local fit to the O VIII Lyα and O VII He-like triplets in the 2000-2001 time-averaged RGS spectrum of NGC 3783. The continuum is fixed to the best-fit global continuum corrected for the foreground Galactic absorption, the warm absorber and the broad emission features.

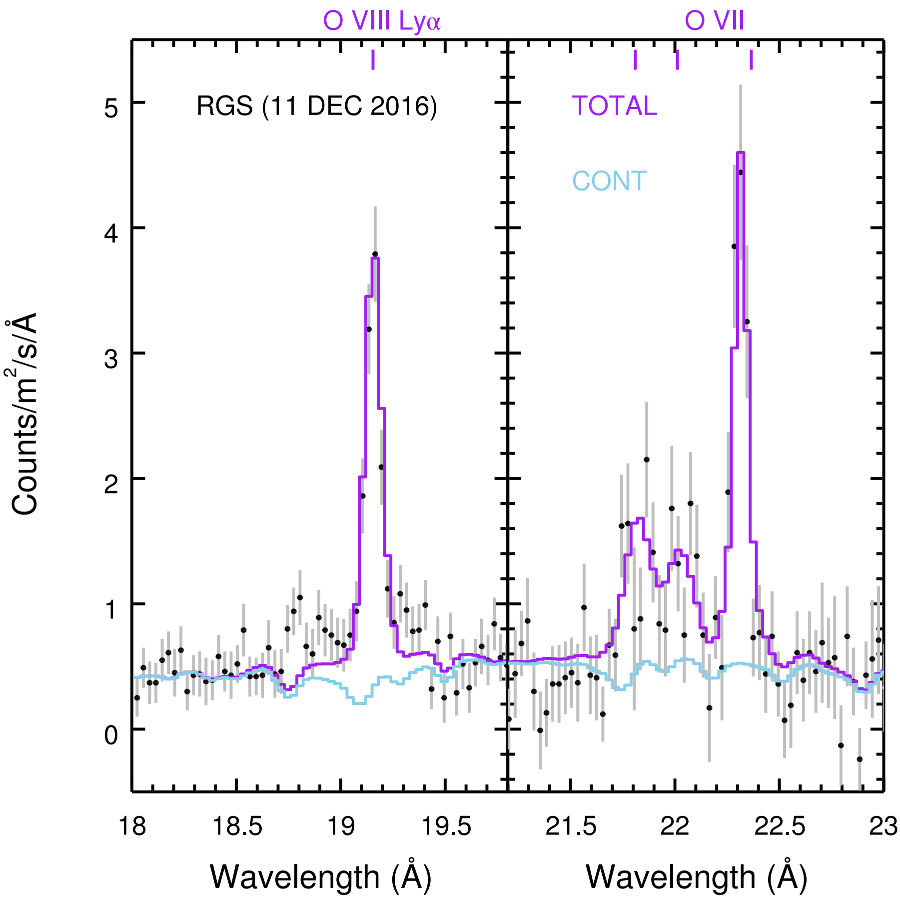

Figure 6.9: Local fit to the O VIII Lyα (left panel) and O VII He-like triplets (right panel) in the RGS spectrum of NGC 3783 from 11 December 2016. The continuum is fixed to the best-fit global continuum corrected for the foreground Galactic absorption, the obscurer, the warm absorber and the broad emission features.

Table 6.5: Best-fit results of the oxygen emission lines from RGS data in 2000–2001 and December 2016.

Ion	Line	2000–2001		11 DEC 2016		21 DEC 2016	
	λ ()	L (10^{32} W)	σ_v (km s^{-1})	L (10^{32} W)	σ_v (km s^{-1})	L (10^{32} W)	σ_v (km s^{-1})
O VIII Lyα	18.97	13.4 ± 0.9	360 ± 130	17.8 ± 1.1	370 ± 100	19.8 ± 1.1	520 ± 130
O VII (r)	21.60	6.6 ± 1.4	< 280	9.2 ± 1.8	740 ± 190	8.4 ± 2.1	< 500
O VII (i)	21.81	1.3 ± 1.3	< 280 (c)	6.0 ± 1.6	740 (c)	5.5 ± 0.6	< 500 (c)
O VII (f)	22.10	18.5 ± 1.7	310 ± 100	17.6 ± 1.9	< 180	17.3 ± 3.1	< 300

Notes. Velocity broadening (σ_v) of the resonance and intercombination lines of O VII are coupled (c) in the fit.

6

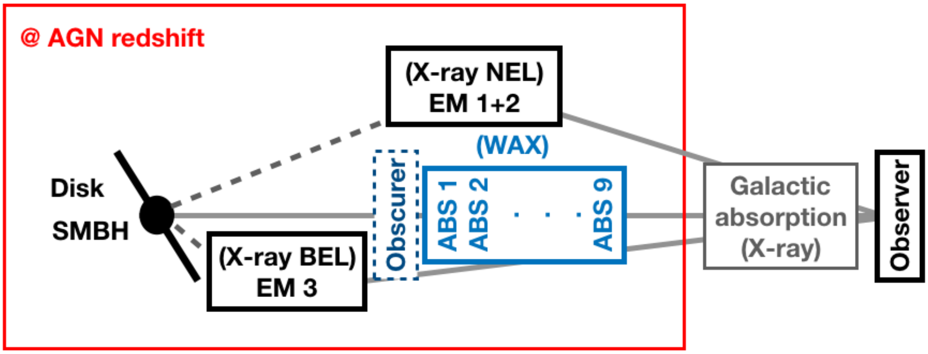

Figure 6.10: Simplified relations of components observed in NGC 3783 in X-rays. Three different light paths are shown here. The obscurer (dashed box) is not always present along the line of sight. Dashed lines indicate that these photons are not directly observable. WAX is short for the warm absorber in X-rays. BEL and NEL refer to the broad and narrow emission line. EM and ABS are short for emission and absorption, respectively.

6

resolution UV spectra with HST in 2000–2001 and December 2016 (Kriss et al. in prep). No significant variation is found in the line flux of Lyα, Si IV, C IV and He II between the two epochs. Hence, our previous assumption of a non-varying X-ray broad emission component is reasonable.

6.4.5. Summary

We analyzed the X-ray spectra of the Seyfert 1 galaxy NGC 3783 using both archival data in 2000–2013 and newly obtained data in December 2016. The intrinsic SED of the AGN, the obscuration, absorption, emission, and extinction effects are fitted simultaneously. In Figure 6.10 we show a sketch of what we think we are looking at.

Along the line of sight toward the nucleus, prominent absorption line features due to the warm absorber were clearly visible in the 2000–2013 X-ray spectra (e.g., Krongold et al. 2003; Netzer et al. 2003; Scott et al. 2014). Nine X-ray absorption components with different ionization parameters and kinematics are required in our photoionization modeling. On 11 and 21 December 2016, obscuration was seen in NGC 3783 (Mehdipour et al. 2017). The obscurer produces the heavy absorption of the soft X-ray continuum, as well as broad and blueshifted absorption lines in the UV spectra. It is very likely that there are more obscuration events in NGC 3783 (Markowitz et al. 2014, , Kaastra et al. 2018). Moreover, obscuration events have also been discovered in NGC 5548 (Kaastra et al. 2014) and NGC 985 (Ebrero et al.

2016).

The X-ray narrow emission components reprocess photons from the nucleus that are not directly observed (dashed lines in Figure 6.10). Prominent emission features like the O VIII Lyα line and the He-like triplets of O VII are visible whether the soft X-ray continuum is obscured or not. Weak emission features like the O VII RRC are detectable only when the continuum is obscured. Our photoionization modeling requires two components for the X-ray narrow emission features in NGC 3783. The two narrow emission components have different emission measure, ionization parameter, turbulence velocity, and emission covering factor. This is similar to our previous analysis for NGC 5548 (Mao et al. 2018).

Our photoionization modeling (Table 6.4) finds that the ionization parameter of the X-ray narrow emission component 1 remains constant throughout 2000–2016, indicating that either this component has a distance of at least a few light-years or its density is very low. On the other hand, for the X-ray narrow emission component 2, the ionization parameters are consistent between the two observations in December 2016 yet about a factor of two lower when compared to 2000–2001. If the variation is due to the change in the ionizing continuum, this suggests that component 2 is closer than component 1, but its distance should be larger than 10 light-days.

The X-ray broad emission component also reprocesses photons from the nucleus. In this work, we demonstrate that, when the obscurer is present in NGC 3783, it screens photons emitted from the X-ray broad emission component, which leads to the apparent weakening of the X-ray broad emission features in December 2016 (Section 6.4.3). The above interpretation supports the geometry proposed by Mehdipour et al. (2017) that the obscurer is located farther away than the X-ray broad emission component, which is a few light days from the nucleus (Peterson et al. 2004). Our photoionization modeling of the observed X-ray broad emission features is an ad hoc interpretation. There is evidence that the optical, UV, and X-ray broad emission lines originate from the same photoionized plasma (e.g., Costantini et al. 2016). Thus, the broad-line region has a range of densities, ionization parameters, and kinematics. A dedicated analysis with the "locally optimally emitting cloud" approach (e.g., Costantini et al. 2007) or even sophisticated dynamic models (e.g., Pancoast et al. 2011) is required to interpret the optical to X-ray broad emission lines in NGC 3783.

For simplicity, we assume that the X-ray broad and narrow emission components are not further absorbed by the warm absorber (Section 6.3.2), which might not be true. That is to say, the unabsorbed luminosity of the X-ray broad and narrow emission lines obtained here is only a lower limit. To properly account for the screening effects by the warm absorber, we need to know which warm absorber components are more distant than the X-ray emission regions, and what are the covering factors for these warm absorber components with respect to the X-ray emission regions.

6.5. Conclusions

We focus on the photoionized emission features in the high-resolution X-ray spectra of NGC 3783 obtained in December 2016 when the soft X-ray continuum was heavily obscured. We also analyze the archival time-averaged high-resolution X-ray spectrum in 2000–2001 to compare the photoionized emission features and study the warm absorber. The main results are summarized as follows.

1. Nine photoionization components with different ionization parameters and kinematics are required for the warm absorber.
2. Two photoionization components are required for the X-ray narrow emission features, which are weakly varying over the past 15 years.
3. The presence of a X-ray broad emission component significantly improves the fit to the time-averaged spectrum in 2000–2001.
4. The X-ray broad emission features are much weaker in December 2016. This apparent weakening can be explained by the obscuration effect on the X-ray broad emission component.

6.A. Component relation in fitting the spectra using SPEX

The Comptonized disk component (COMT in SPEX), the power-law component (POW), the neutral reflection component (REFL) are additive components. An exponential cut-off is applied to the high- and low- energy end of the power-law component. This is realized via the ETAU model in SPEX (see also Chapter 7 of the SPEX cookbook), which provides a simple transmission $T(E) = \exp(-\tau_0\ E^a)$, where τ_0 is the optical depth at 1 keV. For the high-energy cut-off, we set $a = 1$ and $\tau_0 = 1/340$, which corresponds to a cut-off energy at 340 keV (De Rosa et al. 2002). For the low-energy cut-off, we set $a = -1$ and $\tau_0 = T_{\rm seed}$, which corresponds to a cut-off at the seed photon temperature ($T_{\rm seed}$) of the Comptonized disk component.

The warm absorber is modeled with nine PION absorption components, which are multiplicative components. The most highly ionized component (index 1) is assumed to be the closest to the nucleus, while the least ionized component (index 9) is assumed to be the furthest. In the absence of the obscurer, the first PION absorption component is directly exposed to the AGN SED. Ionizing photons received by the second PION absorption is the AGN SED screened by the first PION absorption component. The rest is done in the same manner. In the presence of the obscurer, photons from the nucleus are first screened by the obscurer then modified by PION absorption components.

The PION emission components (for the X-ray photoionized emitter) are both multiplicative and additive. This is because they reprocess ionizing photons which are not directly observed (dashed lines in Figure 6.10) and emit photons which are directly observed. Accordingly, the ionizing continuum is first multiplied by the PION emission components (as multiplicative components) then followed by a ETAU component with $\tau_0 = 1000$ and $a = 0$ so that this ionizing continuum is not present in the spectrum. As additive components, the PION emission components are multiplied by the redshift of the AGN and the Galactic absorption in X-rays.

References

Badnell, N. R. 2006, ApJS, 167, 334

Behar, E., Rasmussen, A. P., Blustin, A. J., et al. 2003, ApJ, 598, 232

Bennert, N., Jungwiert, B., Komossa, S., Haas, M., & Chini, R. 2006a, A&A, 459, 55

Bennert, N., Jungwiert, B., Komossa, S., Haas, M., & Chini, R. 2006b, A&A, 456, 953

Bentz, M. C., Denney, K. D., Grier, C. J., et al. 2013, ApJ, 767, 149

Bianchi, S., Guainazzi, M., & Chiaberge, M. 2006, A&A, 448, 499

Blandford, R. D., Netzer, H., Woltjer, L., Courvoisier, T. J.-L., & Mayor, M., eds. 1990, Active Galactic Nuclei, 97

Blustin, A. J., Branduardi-Raymont, G., Behar, E., et al. 2002, A&A, 392, 453

Canizares, C. R., Davis, J. E., Dewey, D., et al. 2005, PASP, 117, 1144

Chelouche, D. & Netzer, H. 2005, ApJ, 625, 95

Costantini, E., Kaastra, J. S., Arav, N., et al. 2007, A&A, 461, 121

Costantini, E., Kriss, G., Kaastra, J. S., et al. 2016, A&A, 595, A106

De Rosa, A., Piro, L., Fiore, F., et al. 2002, A&A, 387, 838

den Herder, J. W., Brinkman, A. C., Kahn, S. M., et al. 2001, A&A, 365, L7

Denney, K. D., De Rosa, G., Croxall, K., et al. 2014, ApJ, 796, 134

Detmers, R. G., Kaastra, J. S., & McHardy, I. M. 2009, A&A, 504, 409

Ebrero, J., Kriss, G. A., Kaastra, J. S., & Ely, J. C. 2016, A&A, 586, A72

Elvis, M., Wilkes, B. J., McDowell, J. C., et al. 1994, ApJS, 95, 1
Fu, X.-D., Zhang, S.-N., Sun, W., Niu, S., & Ji, L. 2017, Research in Astronomy and Astrophysics, 17, 095
Fukumura, K., Kazanas, D., Shrader, C., et al. 2018, ApJ, 853, 40
Goosmann, R. W., Holczer, T., Mouchet, M., et al. 2016, A&A, 589, A76
Green, J. C., Froning, C. S., Osterman, S., et al. 2012, ApJ, 744, 60
Hönig, S. F., Kishimoto, M., Tristram, K. R. W., et al. 2013, ApJ, 771, 87
Kaastra, J. S. 2017, A&A, 605, A51
Kaastra, J. S. & Bleeker, J. A. M. 2016, A&A, 587, A151
Kaastra, J. S., Detmers, R. G., Mehdipour, M., et al. 2012, A&A, 539, A117
Kaastra, J. S., Kriss, G. A., Cappi, M., et al. 2014, Science, 345, 64
Kaastra, J. S., Mewe, R., Liedahl, D. A., Komossa, S., & Brinkman, A. C. 2000, A&A, 354, L83
Kaastra, J. S., Mewe, R., & Nieuwenhuijzen, H. 1996, in UV and X-ray Spectroscopy of Astrophysical and Laboratory Plasmas, ed. K. Yamashita & T. Watanabe, 411–414
Kaspi, S., Brandt, W. N., George, I. M., et al. 2002, ApJ, 574, 643
Kaspi, S., Brandt, W. N., Netzer, H., et al. 2001, ApJ, 554, 216
Kaspi, S., Smith, P. S., Netzer, H., et al. 2000, ApJ, 533, 631
Kraemer, S. B., Crenshaw, D. M., & Gabel, J. R. 2001, ApJ, 557, 30
Krongold, Y., Nicastro, F., Brickhouse, N. S., et al. 2003, ApJ, 597, 832
Landt, H., Ward, M. J., Steenbrugge, K. C., & Ferland, G. J. 2015, MNRAS, 454, 3688
Liedahl, D. A. & Paerels, F. 1996, ApJ, 468, L33
Lodders, K. & Palme, H. 2009, Meteoritics and Planetary Science Supplement, 72, 5154
Magdziarz, P. & Zdziarski, A. A. 1995, MNRAS, 273, 837
Mao, J. & Kaastra, J. 2016, A&A, 587, A84
Mao, J., Kaastra, J., & Badnell, N. R. 2017a, A&A, 599, A10
Mao, J., Kaastra, J. S., Mehdipour, M., et al. 2018, A&A
Mao, J., Kaastra, J. S., Mehdipour, M., et al. 2017b, A&A, 607, A100
Markowitz, A. G., Krumpe, M., & Nikutta, R. 2014, MNRAS, 439, 1403
Mason, K. O., Breeveld, A., Much, R., et al. 2001, A&A, 365, L36
Mehdipour, M., Kaastra, J. S., & Kallman, T. 2016, A&A, 596, A65
Mehdipour, M., Kaastra, J. S., Kriss, G. A., et al. 2017, A&A, 607, A28
Mehdipour, M., Kaastra, J. S., Kriss, G. A., et al. 2015, A&A, 575, A22
Netzer, H., Kaspi, S., Behar, E., et al. 2003, ApJ, 599, 933
Nicastro, F., Fiore, F., Perola, G. C., & Elvis, M. 1999, ApJ, 512, 184
Onken, C. A. & Peterson, B. M. 2002, ApJ, 572, 746
Pancoast, A., Brewer, B. J., & Treu, T. 2011, ApJ, 730, 139
Peterson, B. M., Denney, K. D., De Rosa, G., et al. 2013, ApJ, 779, 109
Peterson, B. M., Ferrarese, L., Gilbert, K. M., et al. 2004, ApJ, 613, 682
Ramírez, J. M., Bautista, M., & Kallman, T. 2005, ApJ, 627, 166
Scott, A. E., Brandt, W. N., Behar, E., et al. 2014, ApJ, 797, 105
Silva, C. V., Uttley, P., & Costantini, E. 2016, A&A, 596, A79
Smith, R. K., Abraham, M. H., Allured, R., et al. 2016, in Proc. SPIE, Vol. 9905, Space Telescopes and Instrumentation 2016: Ultraviolet to Gamma Ray, 99054M
Strüder, L., Briel, U., Dennerl, K., et al. 2001, A&A, 365, L18
Theureau, G., Bottinelli, L., Coudreau-Durand, N., et al. 1998, A&AS, 130, 333

Titarchuk, L. 1994, ApJ, 434, 570
Zycki, P. T., Done, C., & Smith, D. A. 1999, MNRAS, 305, 231